

Do double ‘SS precursors’ mean double discontinuities?

Zhao Zheng¹ and Barbara Romanowicz^{1,2}

¹Berkeley Seismological Laboratory, University of California, Berkeley, CA 94720, USA. E-mail: zhaozheng@berkeley.edu

²College de France, Paris, France

Accepted 2012 September 18. Received 2012 September 9; in original form 2012 May 10

SUMMARY

Stacks of SS precursors have been widely used in the past two decades to investigate the existence and characteristics of upper mantle discontinuities on a global scale as well as in several regional cases. Here, we present observations of SS precursors from an M_b 6.7 earthquake recorded at the US Transportable Array in 2010. In this particular case, the $S_{660}S$ precursors on the transverse component are strong enough to be identified on individual seismograms across the array without any stacking procedures. Two $S_{660}S$ precursors are observed, seeming to suggest double discontinuities around 660 km depth in the bounce point region. Through careful analysis of 1-D and 3-D synthetic seismograms, we however discover that, although they have arrival times and slownesses that are very close to the theoretical values of SS precursors, the apparent ‘double precursors’ are artefacts because of mantle heterogeneity in the upper mantle near the receivers away from the bounce point region. This suggests that caution must be taken about appropriate azimuthal coverage at the SS bounce point, before interpreting double SS or PP precursors in terms of complex mineralogical transitions.

Key words: Body waves; Wave scattering and diffraction.

1 INTRODUCTION

Two discontinuities, at 410 and 660 km depths approximately, delineate the Earth’s mantle transition zone, which separates the upper and the lower mantle. These discontinuities are widely observed seismically on a global scale and are prominent features in 1-D reference models such as PREM (Dziewonski & Anderson 1981). There is general agreement that they are caused by phase transitions in mantle minerals, in particular olivine to wadsleyite at the 410 km and ringwoodite to perovskite and magnesiowüstite at the 660 km discontinuities (Ringwood 1975; Ito & Takahashi 1989; Ita & Stixrude 1992). The garnet to perovskite transition also plays a role at the 660 discontinuity (Vacher *et al.* 1998). The depths of the discontinuities serve in principle as a ‘thermometer’ to measure the transition zone temperature anomalies (Bina & Helffrich 1994). The Clapeyron slopes of the olivine transitions predict a shallower 410 and deeper 660 in colder (e.g. subduction zone) regions, and the reverse in warmer (e.g. mantle plume) regions. On the other hand, the garnet transition at the 660, though minor, has an opposite sign (Ito *et al.* 1990) to the olivine transition, sometimes complicating the prediction (Herzberg & Gasparik 1991; Weidner & Wang 1998). Detailed characteristics of the discontinuities are crucial for understanding the temperature, composition and dynamics of the mantle. For example, it still remains debatable whether mantle convection is confined to layers or is of whole-mantle scale (Hofmann 1997; Schubert *et al.* 2001). Tomographic studies (e.g. Li *et al.* 2008) have observed stagnant slabs in the transition zone in particular regions such as the northwest Pacific, suggesting that the 660 discontinuity

acts as a barrier for material transfer across it (Ringwood 1994), whereas at some other locations such as Sumatra and Peru, the slabs appear to penetrate through the transition zone and dive directly into lower mantle (Fukao *et al.* 2009). Study of the discontinuities will help to put constraints on such hypotheses.

Seismic constraints on the discontinuities first came from array studies of triplications (e.g. Niazi & Anderson 1965) and converted phases (e.g. Vinnik 1977). Later, receiver functions (e.g. Simmons & Gurrola 2000) and multiple ScS reverberations (e.g. Revenaugh & Jordan 1991) were also employed for detecting the discontinuities. Such data types, however, are restricted by station distribution and usually confined to regional scales. In contrast, the SS (and PP) precursors, which are reflections from the bottom side of the discontinuities (Fig. 1), are able to provide a significant global coverage even for oceanic regions, as their sensitivity is concentrated at the mid-point between the earthquake and the seismic station. Because the ray paths of SS and its precursors are nearly identical outside the bounce point region, common practice has been to measure the differential traveltimes between a precursor and the main phase and then translate it to the discontinuity depth at the bounce point. Crust and upper mantle velocity models are assumed for static traveltime corrections. The amplitudes of the precursors are generally small (5–10 per cent of the main phase), at or below the noise level. Stacking is therefore necessary to enhance the signal. Mid-point stacking over geographical bins with radius of 10° has been common. Pioneered by Shearer (1991), many studies (e.g. Flanagan & Shearer 1998; Deuss & Woodhouse 2002; Gu & Dziewonski 2002;

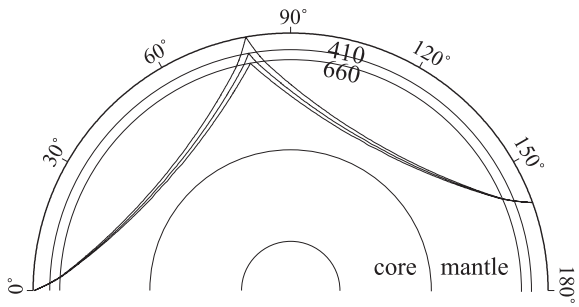


Figure 1. Ray paths of *SS* and its precursors. The precursors are the underside reflections off the upper mantle discontinuities of the Earth. They travel very similar but slightly shorter paths than the main phase *SS* and therefore arrive earlier on seismograms, hence the name ‘precursors’. They are named according to the associated discontinuities, for example $S_{410}S$ and $S_{660}S$.

Houser *et al.* 2008; Lawrence & Shearer 2008) have employed *SS* precursor traveltimes to map discontinuity topography and transition zone thickness on the global scale. These results agree on very long wavelength features, however, considerable discrepancies exist on smaller scales (for a review, see Deuss 2009). In addition to 410 and 660 which are present globally, other discontinuities are observed at 220, 300–350, 520, 800–900 km depths for various regions. On regional scales, the precursor method has also been applied to a few locations where denser coverage allows higher resolution. Such regions include the central Pacific around Hawaii (Schmerr & Garnero 2006; Cao *et al.* 2010, 2011), south America (Schmerr & Garnero 2007; Contenti *et al.* 2012), eastern Asia (Heit *et al.* 2010), Japan and Kurile (Schmerr & Thomas 2011) and north-western Pacific (Gu *et al.* 2012). In addition to *SS* and *PP* precursors, *PP'* (*PKPPKPP*) precursors are sometimes observed (e.g. Le Stunff *et al.* 1995), however, strict requirements on ray path geometry confines their application to very few regions.

2 DATA

The deployment of the US Transportable Array (TA) brings new opportunities to try and resolve finer scale discontinuity characteristics for much broader regions. As a rule of thumb, given the average inter-station distance of 70 km, the spacing between bounce points is half of that, that is 35 km. Here we present an observation of *SS* precursors from an M_b 6.7 earthquake (2010 May; depth 38 km) occurring in northern Sumatra and recorded at the US TA (Fig. 2). The magnitude of this event is optimal in that the precursor signals are strong enough, whereas the source duration is relatively short (~ 10 s) compared to the frequency content of the precursor energy (~ 30 – 40 s). The source time function is fairly simple as revealed by the waveforms of main phases. A shallow depth is chosen to avoid interference between one precursor’s depth phase and the next precursor, as is common practice in precursor studies. The event has a radiation pattern that favours *SS* on the transverse component. All available stations from the TA at the time of the event are used. The epicentral distances fall in the range between 120° and 150° , which is very suitable for an *SS* precursor study. We consider the transverse component displacement seismograms bandpass filtered in the range 20–100 s (shorter periods are also tested). Later, we also take into account the radial component.

In this particular case, the precursor signals are well above noise level on most individual traces throughout the entire array, exempting us from the need of stacking. Fig. 3(a) shows a record section of one particular azimuth range (20° – 23°). The traces are arranged

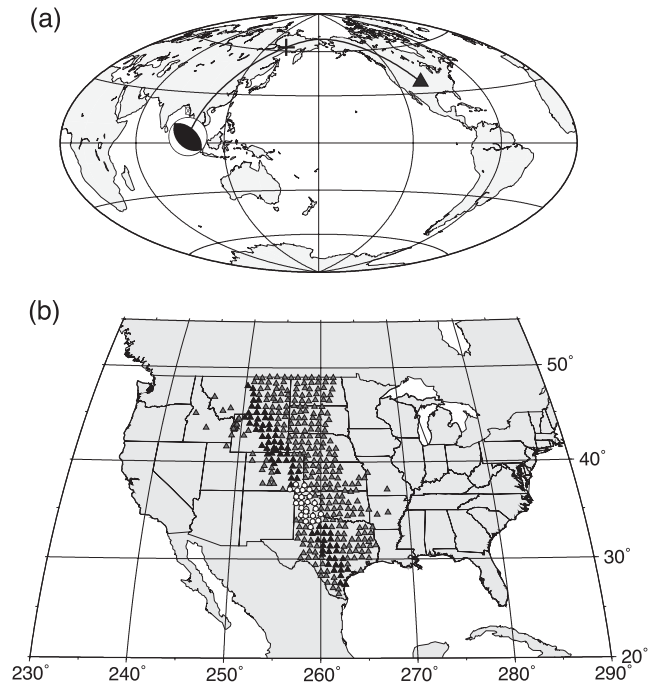


Figure 2. (a) A representative *SS* ray path from the target event to the US Transportable Array (TA) used in this study. The beach ball marks the location and focal mechanism of the event. The triangle marks the approximate location of TA. The cross denotes the bounce point, which is located approximately half way between the source and the receiver. (b) A map of the TA stations (triangles). They are binned by azimuth and distance for further analysis. Black triangles indicate the stations in the azimuth range of 20° – 23° , which are chosen to plot record sections in forthcoming figures. Within this azimuth range, the stations in the distance range of 135° – 140° are shown in white circles.

according to epicentral distance. Two signals around the theoretical $S_{660}S$ arrival time (dots) can be tracked down coherently across the profile. Their amplitudes are anomalously strong compared to PREM prediction (Fig. 3b). Vespagram analysis (Fig. 4) reveals that both signals have a slowness that is close to the theoretical value for *SS* precursors. In conventional interpretation, the double precursors would imply two discontinuity reflectors in the bounce point region. One would further estimate their depths to be around 660 and 810 km, respectively, based on their traveltimes.

3 ONE-DIMENSIONAL AND THREE-DIMENSIONAL MODELLING

We attempt to fit the observations with both 1-D and 3-D modelling. For the 1-D case, synthetics are computed for the PREM model using normal mode summation. The synthetics are bandpass filtered between 20 and 100 s (same as that applied to the observed waveforms). The eigenfunctions for mode summation are complete down to 10 s, which is sufficient for the frequency band we study. A record section of 1-D synthetics is shown in Fig. 3(b). As expected, only one $S_{660}S$ precursor is present, as there is only one 660 discontinuity in the PREM model.

We then conduct 3-D modelling using a tomographic global mantle shear velocity model S362ANI (Kustowski *et al.* 2008) in combination with CRUST2.0 (Bassin *et al.* 2000). The spectral element method (Komatsitsch & Tromp 2002a,b) is employed for computing synthetics that are accurate at periods > 17 s. They are then bandpass filtered between 20 and 100 s, in the same way as applied to

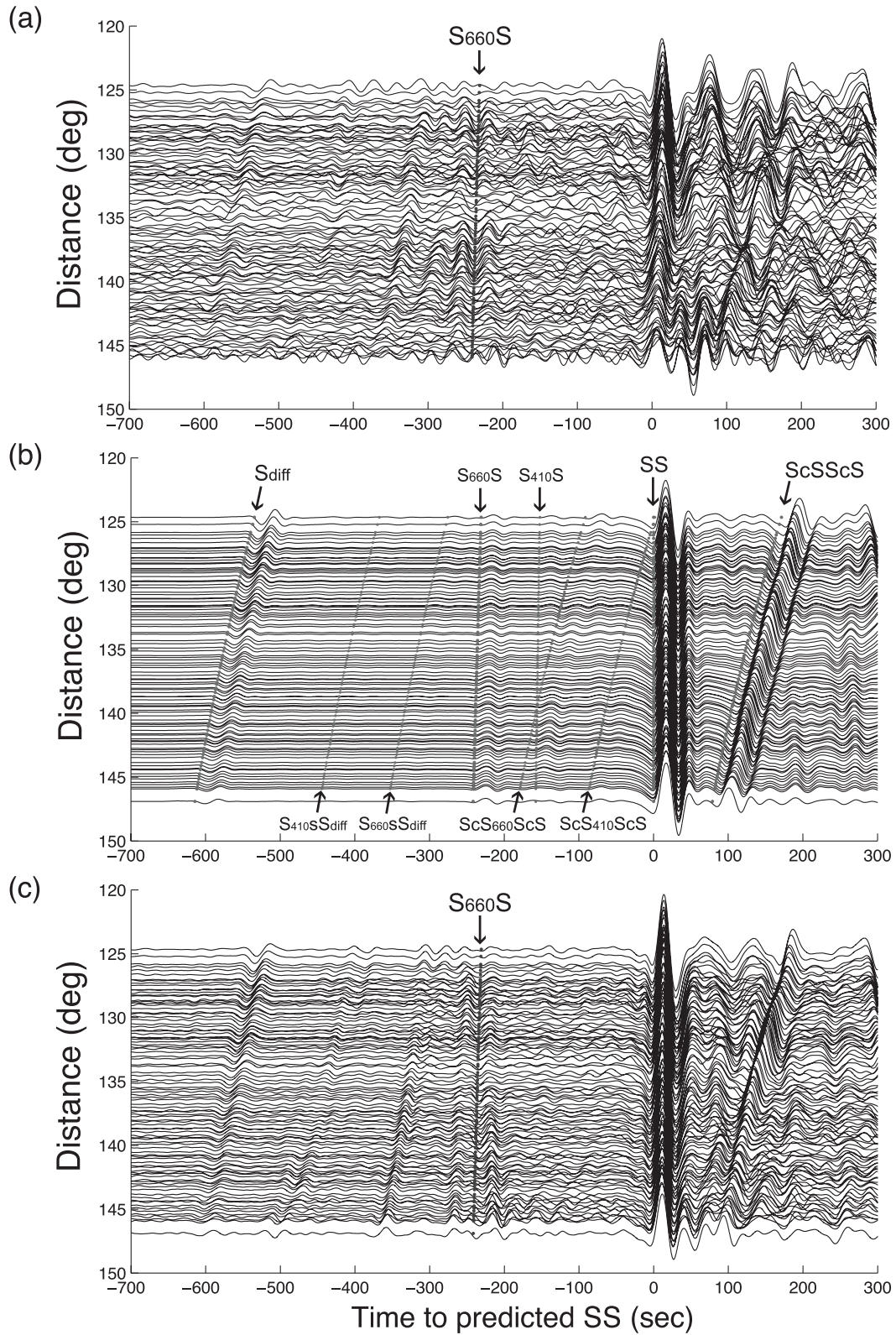


Figure 3. Transverse component record sections of (a) observed waveforms, (b) 1-D synthetics and (c) 3-D synthetics for stations in the azimuth range of 20° – 23° , aligned on the theoretical arrivals of the main phase SS. Major seismic phases and their associated precursors are marked by dotted lines on the 1-D synthetics, for reference. The PREM model (Dziewonski & Anderson 1981) is used to calculate the theoretical arrival times of these phases. The $S_{660}S$ precursors are marked on the observations and 3-D synthetics.

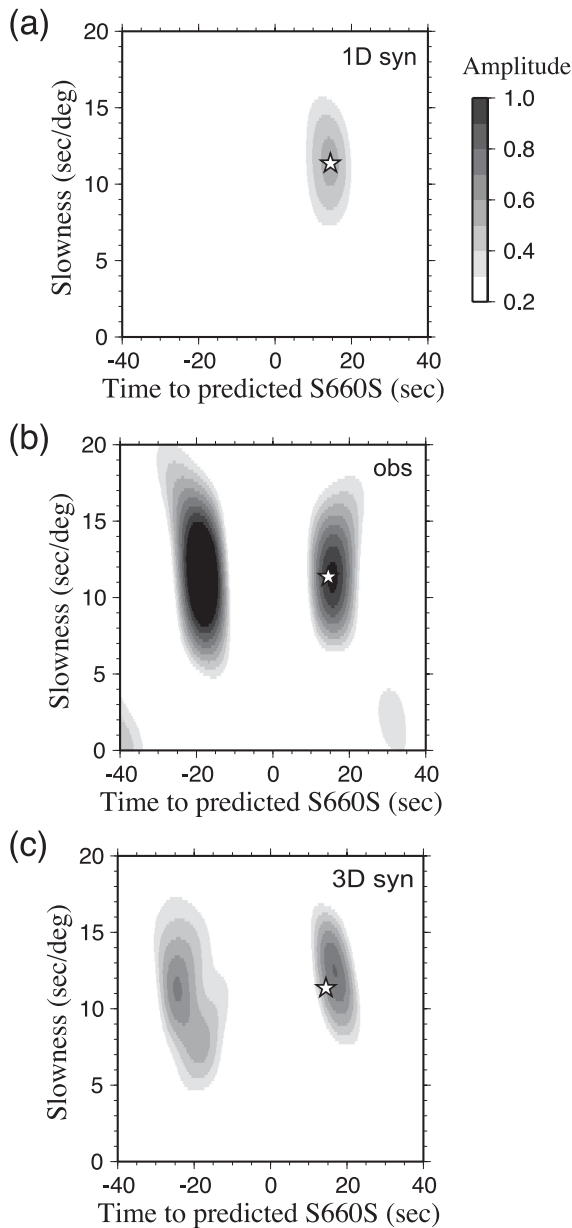


Figure 4. Vespagrams of (a) 1-D synthetics, (b) observations and (c) 3-D synthetics in the $S_{660}S$ precursor time window. A simple slant stacking (linear) technique is used. The stars denote the peak picked from the vespagram of the 1-D synthetics. Its position is in agreement with predictions calculated by the TauP toolkit (Crotwell *et al.* 1999) for PREM. The arrival time indicated by the star is ~ 14 s later than the PREM prediction (0 on the x -axis), which is understood because TauP calculates arrival times at infinitely high frequency (i.e. onset of the phase) whereas the vespagram looks for maximum energy.

the data and 1-D synthetics. The corresponding record section of synthetics is shown in Fig. 3(c). A close inspection of the precursor waveforms (Fig. 5) and the amplitude measurements (Fig. 6) shows that the 3-D synthetics fit the observations much better than the 1-D synthetics. Surprisingly, the 3-D model is capable of producing the double $S_{660}S$ precursors, even though only a single 660 discontinuity is present in the model. This implies that the apparent ‘double precursors’ seen on the 3-D synthetics are produced by heterogeneity rather than double discontinuities at the bounce point. To rule out the possibility of artefacts because of numerical implementation

of the 3-D crust, we have replaced CRUST2.0 with a 1-D layered crust in the simulation and we find the key features in the synthetics do not change. We have also validated our 3-D synthetics by comparison against those provided by the Global ShakeMovie project (<http://global.shakemovie.princeton.edu>; Tromp *et al.* 2010), and they agree perfectly.

It is also noteworthy that the 1-D synthetics fail by far to fit the anomalously large $S_{660}S$ amplitudes as observed, whereas the 3-D model is able to reproduce the amplitudes of both precursors considerably better. As Fig. 6 shows, the 1-D synthetics fail completely (an order of magnitude difference) to predict the amplitudes of the precursor #1, and for #2, the amplitude discrepancy between the observed and the 1-D synthetics is a factor of 2 (a difference of 0.3 on the \log_{10} scale) on average and up to 4 at the maximum. On the other hand, the 3-D synthetics are able to fit the observed amplitudes for both precursors, as well as the pattern (i.e. how amplitude vary with epicentral distance) to a certain degree. To improve the 1-D fit, we have tried other 1-D models with extremely large impedance contrast across the 660 discontinuity, however, they do little to improve the amplitude fits.

In the next step, we test the effect of discontinuity topography (Chaljub & Tarantola 1997), as it is present in the 3-D model S362ANI. We run one more simulation with the same 3-D model except the topographies on the 410 and 660 discontinuities are removed. The synthetics are compared to the model with discontinuity topography for several traces (Fig. 7). The two sets of synthetics look almost identical. In other words, the (long wavelength) undulations of discontinuities have negligible impact on the precursor amplitudes and waveforms at least for the 3-D model considered.

4 NOT BECAUSE OF BOUNCE POINT STRUCTURE?

In the next stage of modelling, we try to pinpoint the structure that is responsible for the ‘double precursors’ seen on the 3-D synthetics. The most probable candidate is certainly the bounce point region. In Fig. 8, a few depth slices of V_{SH} (horizontally polarized shear wave speed) perturbations from the 3-D mantle model S362ANI are shown. The subducted Pacific slab appears to split into two pieces as it dives below 300 km depth. The two pieces pond in the transition zone above the 660 discontinuity, and a ‘slab hole’ is seen in between. The southern piece further extends down to depths greater than 700 km. Based on these images, we conjectured a simple hypothesis (Fig. 9) to explain the double precursors on the 3-D synthetics. In this conceptual model, the specular reflection generates the second (later arrival) $S_{660}S$ precursor, which is also present on 1-D synthetics, whereas the reflection at the bottom of the high velocity slab pieces constitutes the first precursor, which is present on 3-D synthetics and observed traces but not on 1-D synthetics. In more detail, because of the different size and shape of the two slab pieces, their underside reflections are expected to arrive at slightly different times, which would explain the slight split of the first precursor seen on the 3-D synthetics (Fig. 5).

To test this hypothesis, in the next simulation, only the 3-D structure in the vicinity of the precursor bounce point region is preserved (Fig. 10a). In particular, we define a column centred at the approximate centroid of the bounce points, and with a radius of 25° . We keep the velocity perturbations inside the column while we remove the perturbations everywhere outside. A cosine taper is applied at the edge of the column to avoid artefacts because of abrupt cut-off. The synthetics corresponding to this model are shown in Fig. 10(b).

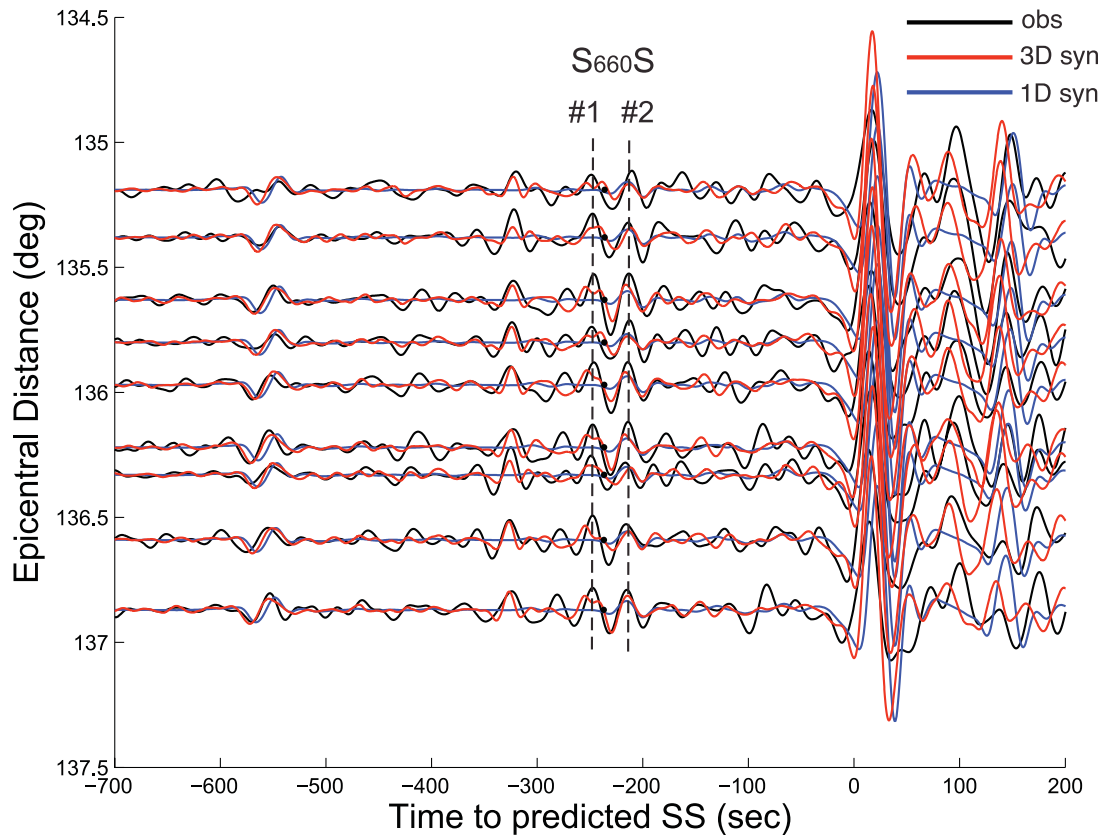


Figure 5. A close-in view of waveform comparison between the observed (black line), the 3-D synthetics (red line) and the 1-D synthetics (blue line). Two coherent phases, labelled #1 and #2, respectively, are identified around the theoretical arrival of the $S_{660}S$ precursor (marked by a dot on each trace) in the observed traces. This observation of 'double precursors' is predicted by the 3-D synthetics, despite the slight split of the #1 phase. In contrast, the 1-D synthetics are flat in the time window of the #1 phase.

To our surprise, the 'double precursor' phenomenon disappears. We try to vary the radius of the column as well as the smoothness of the taper, but there is always only one $S_{660}S$ precursor present. The amplitudes of the precursor are also small. Overall, this set of synthetics has very similar characteristics as in 1-D.

Because bounce point structure is not capable of reproducing the double precursors, we turned to the receiver side. Fig. 10(c) shows a slice (depth at 125 km) of the 3-D model S362ANI in North America. Indeed, a sharp contrast between the fast craton east of the Rocky Mountain Front and the slower western United States is present in the North American upper mantle, a prominent feature also seen in numerous continental scale tomography studies (e.g. van der Lee & Frederiksen 2005; Marone *et al.* 2007; Nettles & Dziewonski 2008; Yuan *et al.* 2011) although a more detailed geometry of the boundary is resolved in the regional models because of higher resolution. Moreover, the boundary between the fast and slow regions is subparallel to the great circle paths for the event studied here. In the following simulation, we preserve only the receiver side upper mantle structure in the 3-D model (Fig. 10c), and the corresponding synthetics are shown in Fig. 10(d). This set of synthetics turns out to be capable of reproducing the 'double precursors'. To confirm that the apparent 'double precursors' are indeed associated with the velocity boundary, we constructed another model (Fig. 10e) in which the boundary is significantly shifted eastwards whereas its orientation still tracks the great circle ray path direction. In this simulation we also expanded the array of virtual receivers to the entire United States to cover a broad range of azimuths across the boundary. The locations of the receivers are taken

from the TA stations, past, present and future. The synthetics from this simulation are shown in Fig. 10(f), arranged by increasing azimuth (from east to west roughly). It is seen that for receivers far away from the boundary (azimuth $< 8^\circ$ or $> 20^\circ$) there is only one precursor (the later one); whereas the other wiggle (the earlier one) picks up when the receivers approach the boundary (azimuth around 14°). These experiments imply that apparent 'double precursors' do not necessarily require double discontinuities or even any complex structure at the bounce point, as commonly assumed by previous precursor studies. Mantle heterogeneities away from the bounce point region are able to generate similar features, which could be very misleading if care is not taken.

We note that we also tested a source-side model in a similar way, but it fails to produce double precursors.

5 NOT SS PRECURSORS?

So far we have focused our analysis on the transverse component. We here consider the radial component. As shown in Fig. 11, on the radial component, both 'precursors' are present with much larger amplitudes than the transverse (a factor of > 4), whereas the SS main phase has amplitudes that are smaller than those on the transverse component. This disproportionality suggests the possibility that the two 'precursors' (previously identified by arrival times and slownesses, which is common practice in precursor studies) are in fact not precursors.

To explain these observations, we consider possible body wave phases that have similar traveltimes. In Fig. 12, the theoretical

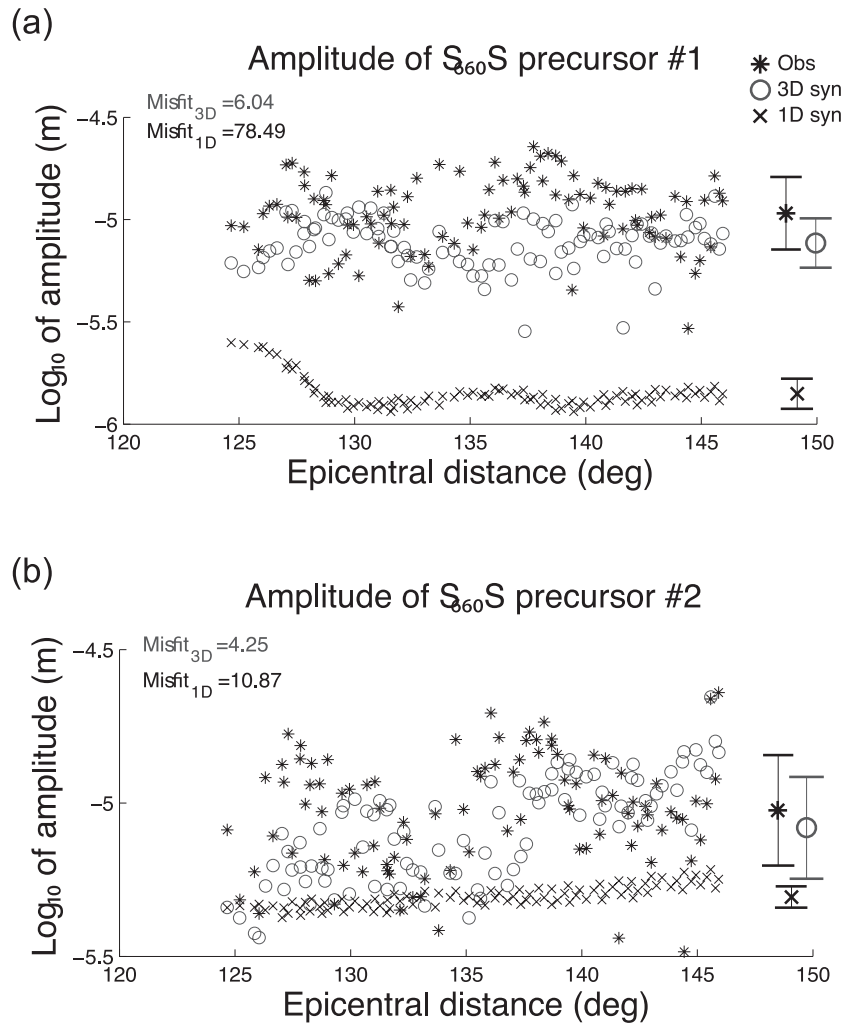


Figure 6. Measurements of the $S_{660}S$ precursor amplitude as a function of epicentral distance for the observations (stars), 3-D synthetics (circles) and 1-D (crosses), in the time windows of (a) precursor 1 and (b) precursor 2. The azimuth range of 20° – 23° is chosen for the measurements. The error bars on the right show the mean and standard deviation from the observations, 3-D and 1-D synthetics, respectively. Misfits by 3-D and 1-D synthetics are listed at the top left of each panel. The misfit is defined as $\sum_i |\log_{10} A^0_i - \log_{10} A^1_i|$, where i is the index of trace, A^0 is the amplitude measured from observed and A^1 measured from 1-D or 3-D synthetics. The larger 1-D amplitudes of precursor #1 at distance $< 128^\circ$ is because of interference of $S_{660}S_{\text{diff}}$ (labelled on Fig. 3b).

arrivals of PPS , $PPPS$, $PPPPS$ and $PPPPPS$ phases (referred to as $P(n)S$ hereafter) are marked. They fit the arrival times of the ‘precursors’ on the radial component reasonably well. These are supposedly SV energy and should not be expected on the transverse component (indeed they are not present on the 1-D synthetics). In this particular setting, however, as the ray paths graze the velocity boundary, because of off-great-circle reflection and refraction, some SV energy could possibly leak to the transverse component, thus generating the apparent ‘precursors’. The arrival times and slownesses of these $P(n)S$ phases are close enough to the SS precursors, leading to the phase misidentification. This is not to say an $S_{660}S$ precursor is not present, but the real precursor (there should be only one, because only one 660 discontinuity is present in the 3-D models) is strongly contaminated or buried by the interfering energy. In fact, the high similarity between the radial and transverse component waveforms in the precursor time window (see Fig. 11) seems to suggest that the energy leaked from the radial component is dominant over the real precursor on the transverse component. The phases arriving ~ 40 s after the expected SS on the radial component can be understood similarly as $P(n)SS$.

Particle motion analysis (Fig. 13) of the ‘precursors’ further confirms our inference that they are artefacts associated with the velocity boundary. As shown by Fig. 13(a), the particle motions of the 1-D synthetics (top row) appear to be radially polarized (i.e. no or near zero motion on the T component) for all the azimuth bins, whereas the trajectories of the observed traces (middle row) and 3-D synthetics (bottom row) both show a ‘tilt’ (i.e. non-zero motions on both R and T components). Fig. 13(b) shows the particle motion of the 3-D synthetics from the modified receiver-side 3-D model (Fig. 10e). The effect of the velocity boundary (located at azimuth $= 14^\circ$) is demonstrated by how the particle motion pattern changes with the azimuth. The ‘tilt’ of the particle motion pattern appears, peaks and disappears as the receivers approach, pass and leave the velocity boundary. These particle motion trajectories show no or minimal ellipticity, which suggests that anisotropy does not play an important role compared to the effect of the boundary.

6 DISCUSSION

Unlike the 410, the 660 discontinuity has been known to exhibit a higher level of complexity (see Deuss 2009 for a review). Multiple

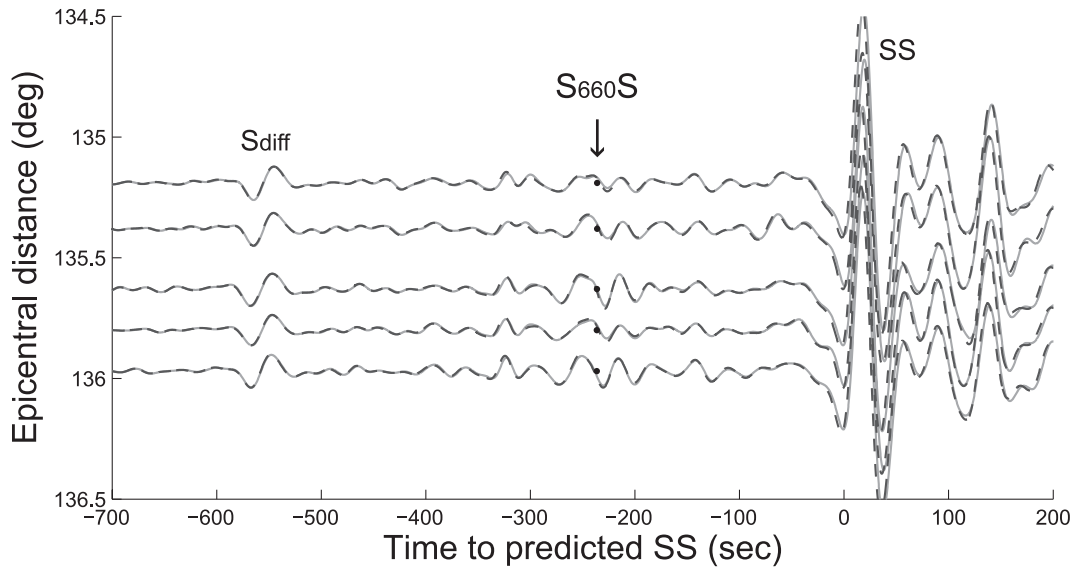


Figure 7. Comparison of synthetics from a 3-D simulation in which the discontinuity topography is present (solid line) versus one in which the topography is removed (dashed line). The dots denote theoretical arrivals of S_{660S} .

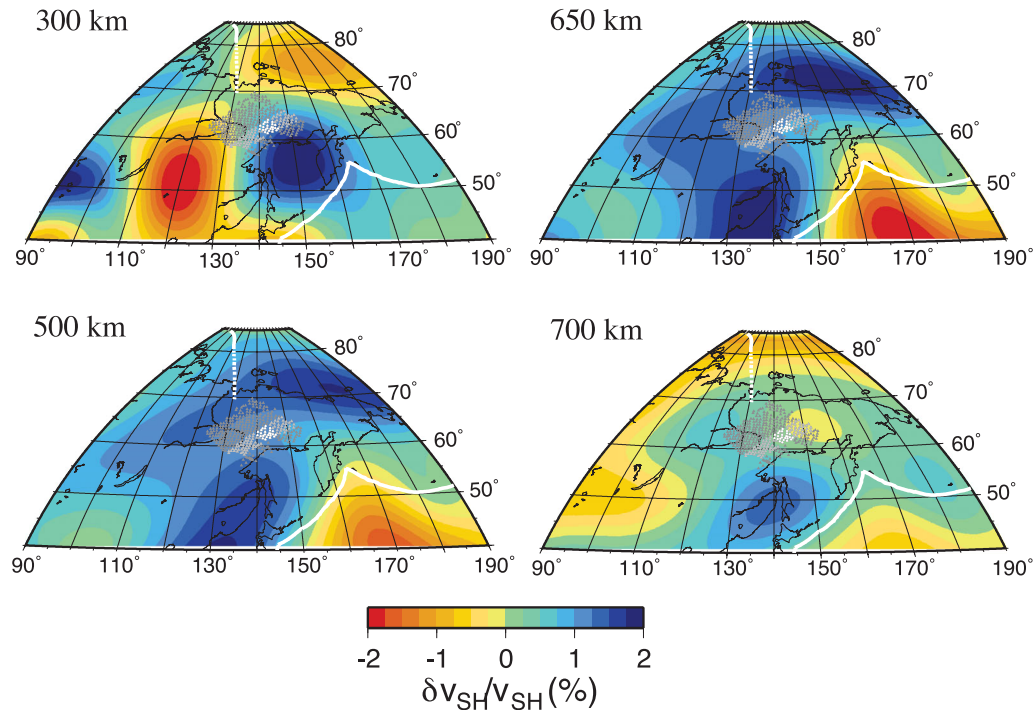


Figure 8. Depth slices of 3-D mantle tomography model S362ANI (Kustowski *et al.* 2008) in the SS bounce point region (the northern bank of Okhotsk Sea). The white curves delineate plate boundaries. The grey dots denote precursor bounce points. Light grey dots correspond to stations in the azimuth range of 20°–23°; white ones stations in the distance range of 135°–140°.

discontinuities around and deeper than 660 km depth have been observed at several locations by various data types and methods. For instance, from P to S receiver functions (0.3 Hz), Simmons & Gurrola (2000) discovered a laterally continuous discontinuity at ~ 720 – 750 km depths beneath southern California, which they inferred to be garnet to perovskite transformation. Andrews & Deuss (2008) assembled a global dataset of P to S receiver functions (0.01–0.02 Hz; 0.02–0.5 Hz), in which about half of the stations show a complex 660 signal, either a broadened single peak or a main 660 accompanied by a smaller, deeper peak in the depth range

710–860 km. They modelled the observations with a combination of a sharp discontinuity representing the olivine dissociation and velocity gradients from the garnet transformation. Deuss *et al.* (2006) collected a global PP precursor dataset and discovered double peaks at 660 and 720 km, for a few locations (such as Canada), when the PP stack is filtered at shorter periods (8–75 s). Using migration of high frequency PP precursors, Thomas & Billen (2009) detected a split 660 in Molucca Sea region with the deeper discontinuity at 690–710 km. Using a similar method, Scharrer & Thomas (2011) detected an intermittent secondary reflector at >800 km depth at

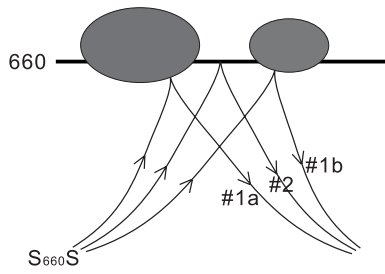


Figure 9. A schematic illustration of the ‘slab hole’ concept (vertical section view), which fails to explain the double precursors produced on the 3-D synthetics. The two shaded blobs represent the two slab pieces ponding on the 660 km discontinuity, as revealed by the 3-D model S362ANI.

certain locations in the Kurile subduction zone. In a review paper, Deuss (2009) provided depth histograms of reflectors detected by global *SS* and *PP* precursors. The histogram of *SS* shows a local maximum at around 800 km depth. Indeed, stacks for a variety of regions show robust reflectors at this or slightly greater depths. For example, the stack for Asia shows a strong reflector at 850 km (from *SS*) or 820 km (from *PP*), and the one for the Indian Ocean has a strong reflector at 800 km from *SS* precursor analysis, but its amplitude is much weaker from *PP* precursors.

Although the split 660 (additional discontinuity with depth up to 720 km) has often been interpreted as because of a phase transition in garnet, the additional discontinuities at greater depths (800–850 km) lack a good explanation (Deuss 2009). The mechanism revealed by this study provides a possible way to understand at least some of these observations. It is noteworthy that the artificial $S_{660}S$ (the

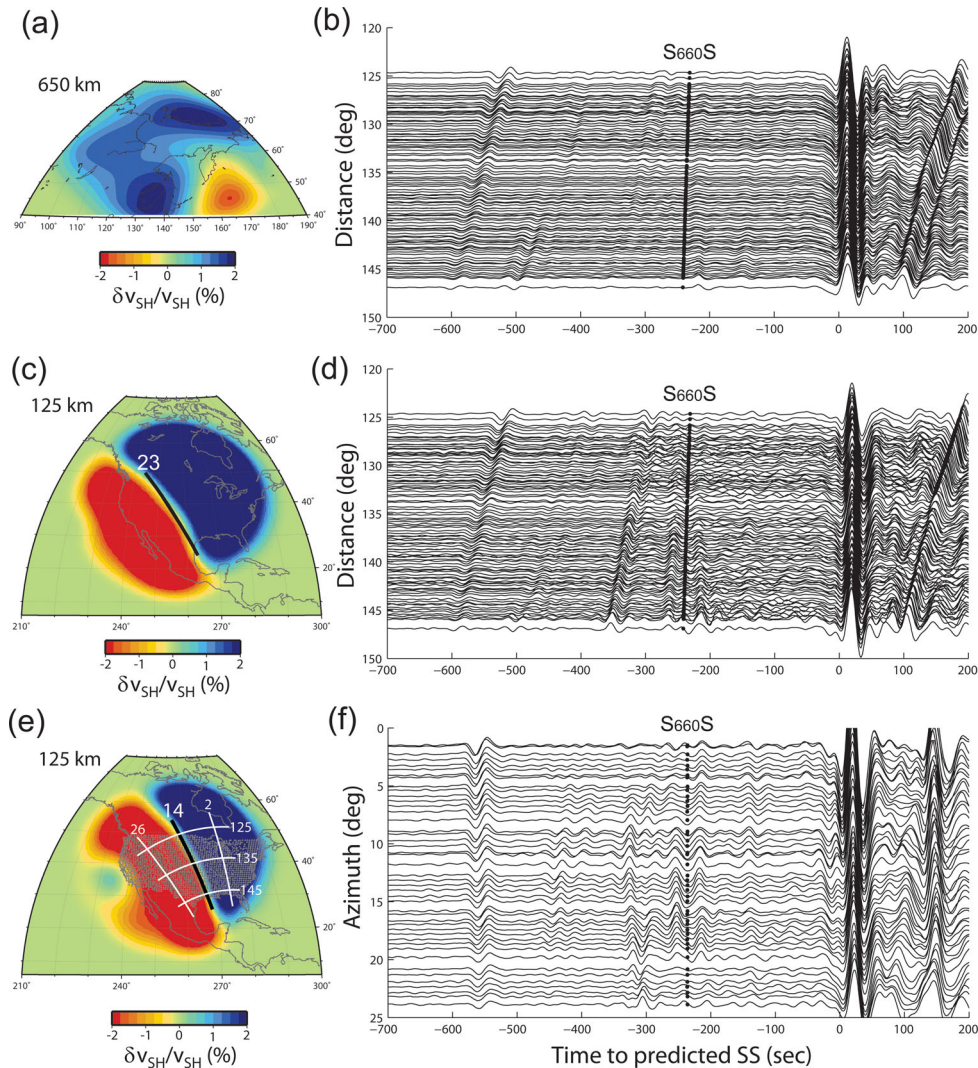


Figure 10. Results of 3-D modelling: velocity models (left panels) modified from S362ANI and corresponding synthetics (right panels). The top row displays a model in which only 3-D structures in the precursor bounce point region are preserved. The middle row shows a model in which only upper mantle structures near the receivers are preserved. A clear velocity boundary between the slower western United States (red) and the faster craton (blue) on the east is seen. The orientation of the boundary roughly follows the great circle track with an azimuth of 23° (black thick line). The bottom row shows a model modified from the middle row one, in which the velocity boundary is shifted eastwards to follow the great circle track at 14° azimuth (black thick line). An expanded set of virtual receivers (grey dots) is used in this simulation, the locations of which are taken from the TA, past, present and future stations. The thick lines indicate equiazimuth (2° , 14° and 26°) and equidistance (125° , 135° and 145°) curves. In (b) and (d), the synthetic traces in the azimuth range of 20° – 23° are plotted, sorted by epicentral distance. In (f), the synthetics are arranged by azimuth for all receivers in the distance range of $135 \pm 1^\circ$.

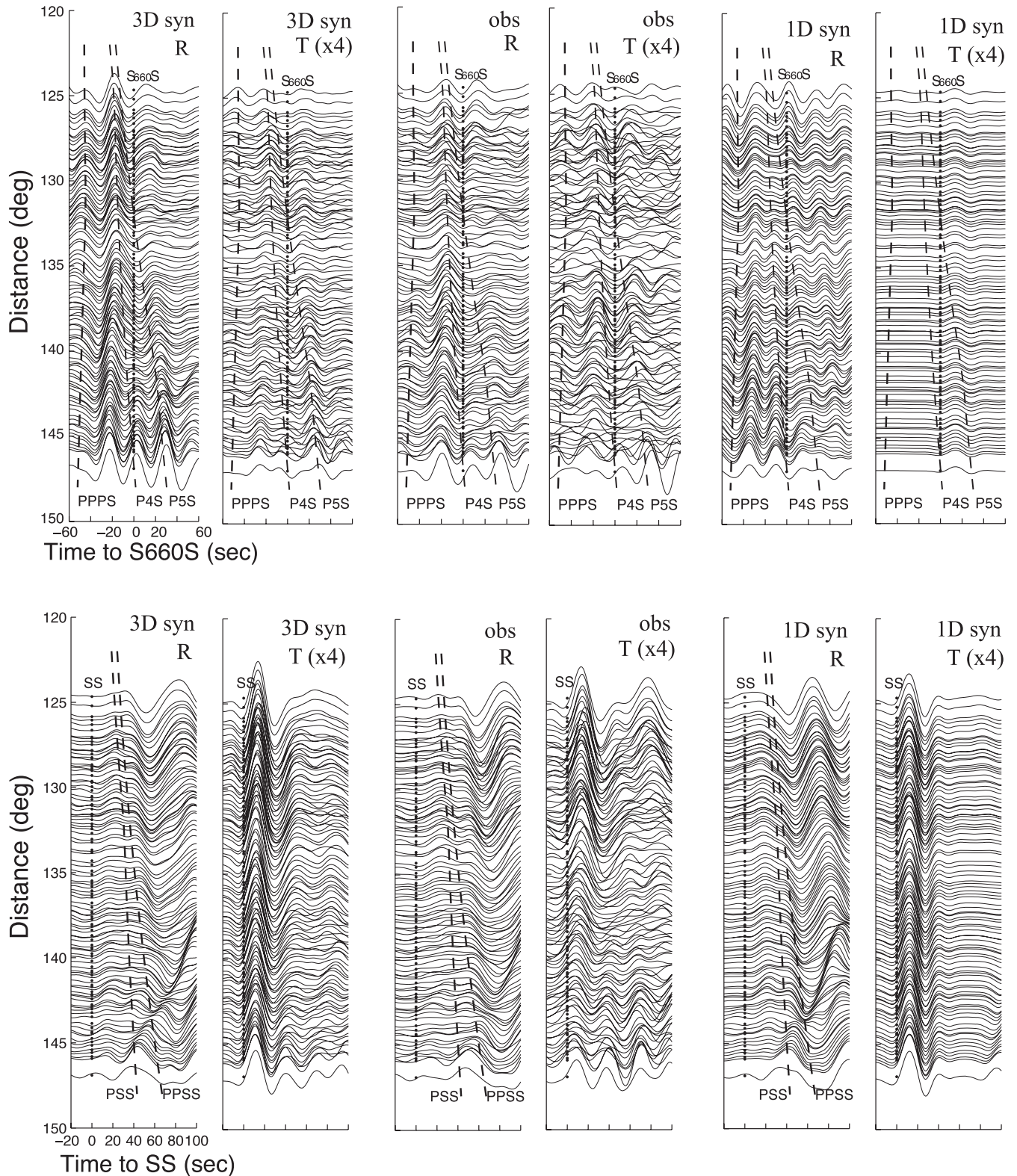


Figure 11. Comparison of radial and transverse component waveforms in the $S_{660}S$ (top) and SS (bottom) time windows for 3-D synthetics, observations and 1-D synthetics. The transverse component amplitudes are blown up by a factor of 4. The $S_{660}S$ and SS theoretical arrivals are marked by dotted lines, and the $PPPS$, $P4S$, etc. phases by dashed lines.

earlier one of the double 'precursors') in this study translates to a discontinuity at approximately 810 km depth. It would have been interesting to examine the PP precursors for this same event, as they are relatively unlikely to be affected by the artefact mechanism

proposed. However, given the epicentral distances considered, the PP precursors are severely interfered with other phases of much larger amplitudes, making the observations of PP precursors not possible.

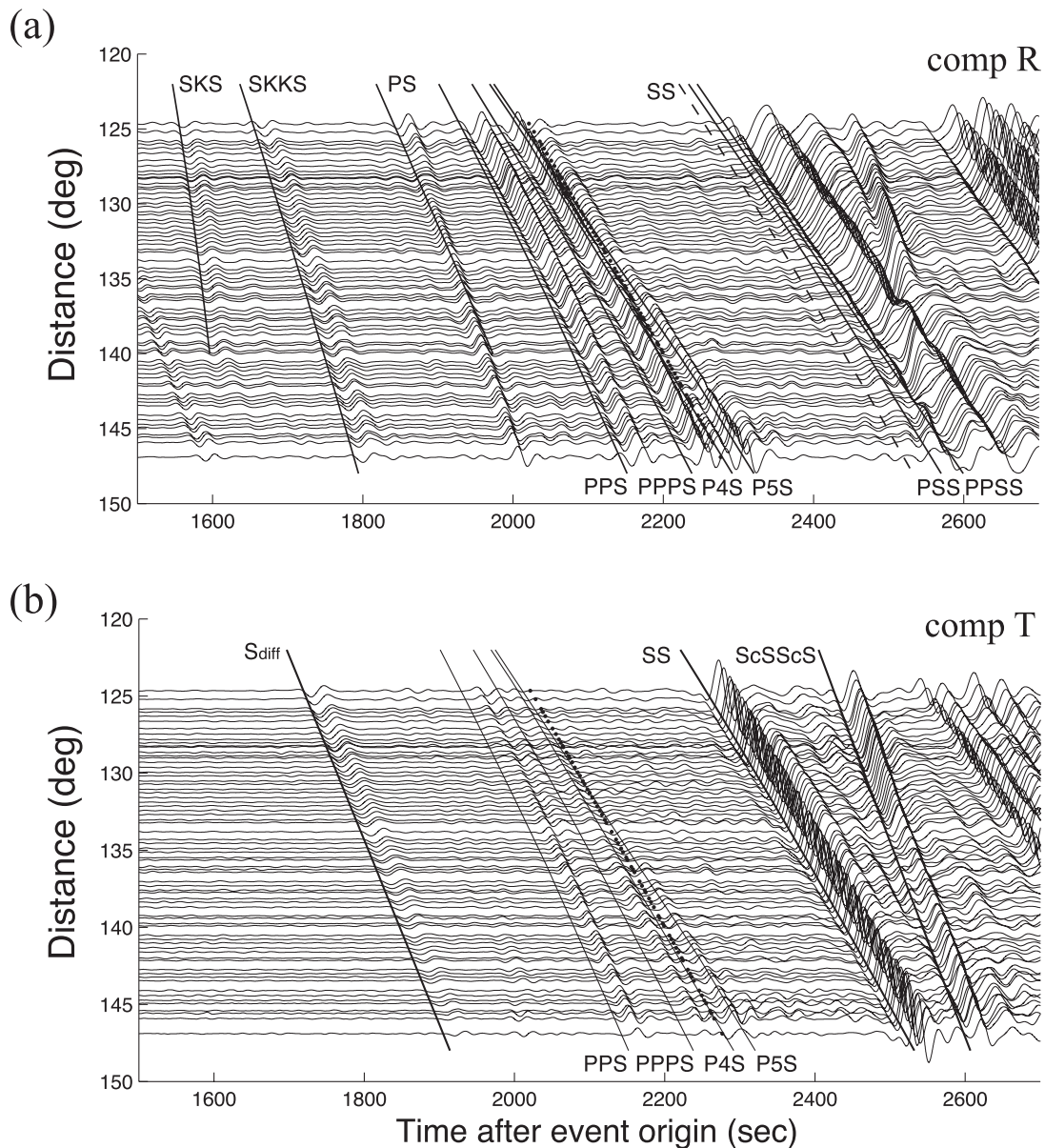


Figure 12. Record sections of 3-D synthetics on (a) the radial and (b) the transverse components, aligned on the event origin time. Theoretical arrivals of major phases are marked by solid lines. The dotted line indicates the expected $S_{660}S$ arrivals.

In addition to the event studied here, we have also analysed a few more events at nearby locations (within 2° away from this event). Because of their either smaller (therefore lower signal-to-noise ratio) or larger (therefore longer and more complicated source time function as well as more signal-generated noise) magnitudes, it is not possible to identify precursors on individual traces across the array as done for this event. Nevertheless, we have looked at the noise free 3-D synthetics made available from the Global ShakeMovie project, and the synthetics indeed exhibit a very similar feature of apparent ‘double precursors’ as seen for this event.

This study suggests that one should be cautious in the interpretation of conventional SS precursor traveltimes studies. The observation of apparent ‘double precursors’ may not necessarily require double discontinuities at the bounce point. In fact, it may not even indicate any complex structure in the bounce point region. Mantle

heterogeneities away from the bounce point region are able to generate artificial ‘precursors’ systematically across a vast area, which can be very misleading if care is not taken when interpreting them. Such artefacts could not be remedied by a static traveltimes correction in stacking (Fig. S1). In addition to multipathing as shown in this study, other mechanisms such as upper mantle anisotropy could also play a similar role in leaking energy to the transverse component.

In the past, a few studies (Zhao & Chevrot 2003; Lawrence & Shearer 2008; Bai *et al.* 2012) have attempted to address the importance of 3-D heterogeneities, however, the focus has been on how much the 3-D structures would perturb the precursor traveltimes measurement, but no attention has been paid to precursor phase identification itself. Moreover, in these studies, the effect of 3-D structure on the precursor traveltimes have been studied and

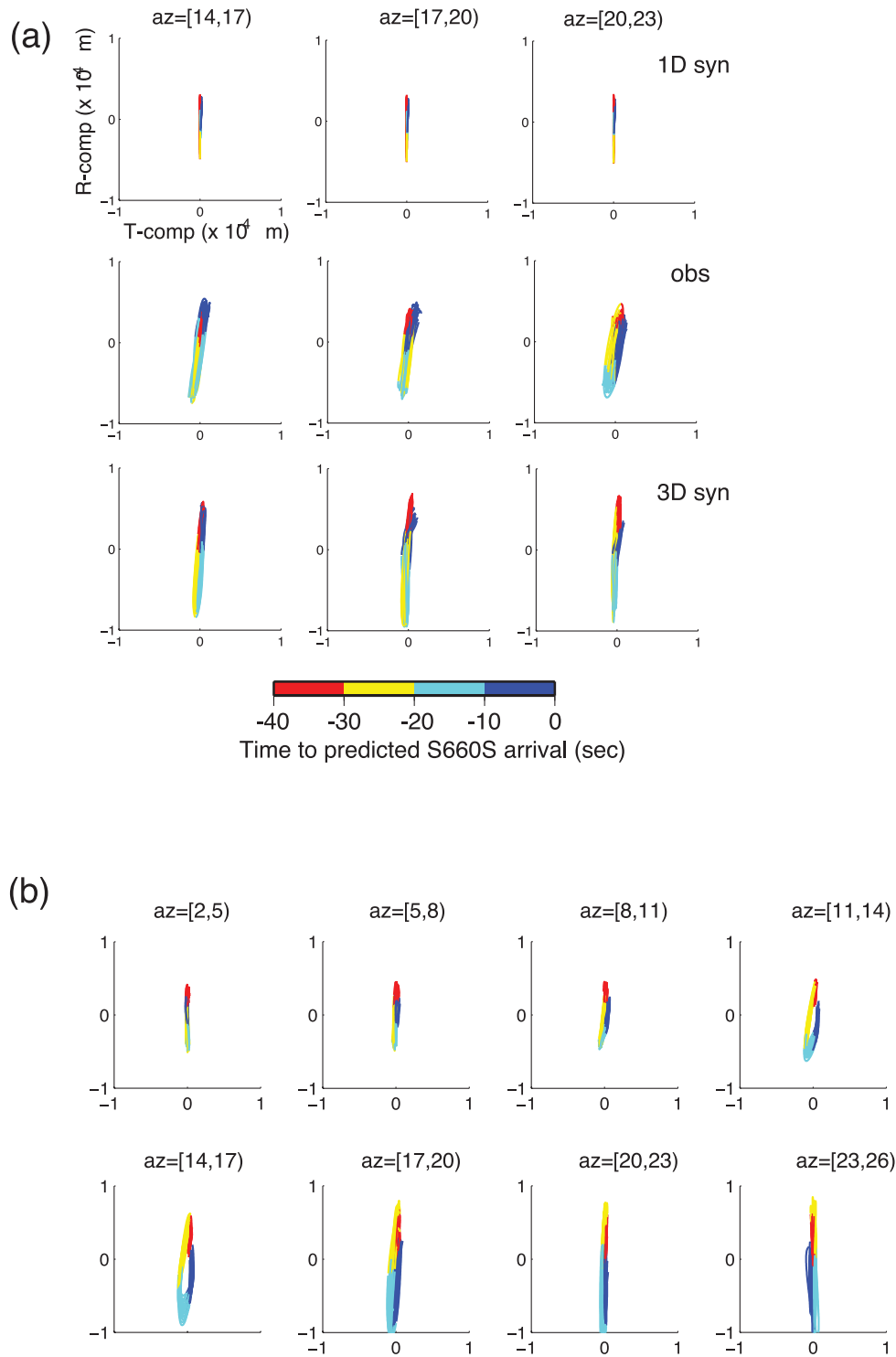


Figure 13. (a) Particle motions (radial versus transverse component displacements) of the 1-D synthetics (top row), observations (middle) and 3-D synthetics (bottom) in the precursor time window. The colour bar shows time elapsed. Different columns from left to right show results for three different azimuth bins. (b) Particle motions of the synthetics from the 3-D model in which the velocity boundary is shifted (Fig. 10e), arranged by increasing azimuths. The velocity boundary in the model approximately follows the azimuth = 14° great circle path.

presented in a statistical framework, therefore, it was not clear exactly which part of the 3-D heterogeneities affect the behaviour of the precursors, and how. Our study provides a new perspective.

Admittedly, the case considered in this study corresponds to a specific ray path geometry that is subparallel to the orientation of the heterogeneity boundary. Nevertheless, it constitutes a valid

warning concerning the usage of array data such as from USArray. For regions such as the one in this study (Okhotsk Sea), other data types (receiver functions, triplications, $P'P'$ precursors, etc.) are not available because of sparsity of seismic stations, so that SS/PP precursors would be the main tool for studying mantle discontinuities. Because of an overwhelming number of stations, the USArray could

dominate the *SS* precursor stack and possibly lead to erroneous conclusions about the transition zone and slab structure in the region. As much as the USArray provides hope for improving resolution of precursor studies, attention must be given to contamination by upper mantle effects on the station side. The same applies to studies based on other regional arrays. One fact worth pointing out is that when smaller seismic arrays are designed, they oftentimes follow local geology to enhance signal coherence (e.g. the Grafenberg array), which might potentially give rise to artefacts as described in this study.

SS precursor studies before the days of USArray might also suffer from the described problem, to some degree. Global studies are probably less affected, owing to more or less even azimuthal coverage in many regions (Fig. S2).

7 CONCLUSIONS

We present observations of *SS* precursors (reflections off the bottom side of upper mantle discontinuities at midpoint) from an M_b 6.7 earthquake recorded at the US TA. In this particular case, we observe apparent ‘double $S_{660}S$ precursors’, both strong enough to be visible on individual seismograms coherently across the array. We compute 1-D and 3-D synthetic seismograms, and find that the 3-D synthetics fit the observations significantly better than the 1-D synthetics. We discover that the ‘double precursors’ are seen on the 3-D synthetics, even though only one 660 discontinuity is present in the earth model. Through further modelling, we confirm that the ‘double precursors’ on the 3-D synthetics are not generated because of double discontinuities at the bounce point, but rather by scattering at a sharp velocity boundary on the receiver-side with an orientation subparallel to the great circle ray paths. We also find that neither are ‘*SS* precursors’, but most likely SV energy leaked from the radial component because of heterogeneity. The real $S_{660}S$ precursor is buried in the second apparent ‘precursor’.

Through numerical 3-D modelling of the precursor waveforms, we have found that apparent *SS* precursors may not necessarily reflect the characteristics of mantle discontinuities in the bounce point region, as often assumed by conventional precursor traveltimes studies. Heterogeneities away from the bounce point region are able to generate artificial ‘precursors’ in a coherent and therefore misleading way. This raises a caution for identifying and interpreting *SS* (and perhaps *PP*) precursors.

We note that this analysis has only been possible because of the possibility of computing highly accurate numerical synthetics in a 3-D earth model, a recent development in global seismology (Komatitsch & Vilotte 1998; Komatitsch & Tromp 2002a,b). We also note that, even though current global tomographic models are still relatively smooth, they are accurate enough to reproduce some of the effects of structural boundaries on seismic body wave propagation. Finally, we recognize that the USArray allows unprecedented density of ray coverage both in azimuth and distance, albeit in limited ranges.

ACKNOWLEDGMENTS

The authors would like to thank Editor Christine Thomas and two anonymous reviewers for very constructive comments. Waveform data used in this study were obtained from the IRIS data center. We thank Scott French for help with the computation of the SPECFEM synthetics. This is BSL contribution 12-13. This work was supported by NSF EAR grant # 0738284.

REFERENCES

- Andrews, J. & Deuss, A., 2008. Detailed nature of the 660 km region of the mantle from global receiver function data, *J. geophys. Res.*, **113**, doi:10.1029/2007JB005111.
- Bai, L., Zhang, Y. & Ritsema, J., 2012. An analysis of *SS* precursors using spectral-element method seismograms, *Geophys. J. Int.*, **188**, 293–300.
- Bassin, C., Laske, G. & Masters, G., 2000. The current limits of resolution for surface wave tomography in North America, *EOS, Trans. Am. geophys. Un.*, **81**, F897.
- Bina, C. & Helffrich, G., 1994. Phase transition Clapeyron slopes and transition zone seismic discontinuity topography, *J. geophys. Res.*, **99**, 15 853–15 860.
- Cao, Q., Wang, P., van der Hilst, R.D., de Hoop, M.V. & Shim, S.-H., 2010. Imaging the upper mantle transition zone with a generalized Radon transform of *SS* precursors, *Phys. Earth planet. Inter.*, **180**(1–2), 80–91.
- Cao, Q., van der Hilst, R.D., de Hoop, M.V. & Shim, S.-H., 2011. seismic imaging of transition zone discontinuities suggests hot mantle west of Hawaii, *Science*, **332**, 1068–1071.
- Chaljub, E. & Tarantola, A., 1997. Sensitivity of *SS* precursors to topography on the upper-mantle 660-km discontinuity, *Geophys. Res. Lett.*, **24**, 2613–2616.
- Contenti, S., Gu, Y.J., Ökeler, A. & Sacchi, M.D., 2012. Shear wave reflectivity imaging of the Nazca-South America subduction zone: Stagnant slab in the mantle transition zone?, *Geophys. Res. Lett.*, **39**, L02310, doi:10.1029/2011GL050064.
- Crotwell, H.P., Owens, T.J. & Ritsema, J., 1999. The *TauP* Toolkit: Flexible seismic travel-time and ray-path utilities, *Seism. Res. Lett.*, **70**, 154–160.
- Deuss, A., 2009. Global observations of mantle discontinuities using *SS* and *PP* precursors, *Surv. Geophys.*, **30**, 301–326.
- Deuss, A. & Woodhouse, J.H., 2002. A systematic search for upper mantle discontinuities using *SS*-precursors, *Geophys. Res. Lett.*, **29**, 901–904.
- Deuss, A., Redfern, S.A.T., Chambers, K. & Woodhouse, J.H., 2006. The nature of the 660-km discontinuity in Earth’s mantle from global seismic observations of *PP* precursors, *Science*, **311**, 198–201.
- Dziewonski, A.M. & Anderson, D.L., 1981. Preliminary reference Earth model, *Phys. Earth planet. Inter.*, **25**, 297–356.
- Flanagan, M.P. & Shearer, P., 1998. Global mapping of topography on transition zone velocity discontinuities by stacking of *SS* precursors, *J. geophys. Res.*, **103**(B2), 2673–2692.
- Fukao, Y., Obayashi, M., Nakakuki, T. & Deep Slab Project Group, 2009. Stagnant slab: a review, *Annu. Rev. Earth planet. Sci.*, **37**, 19–46.
- Gu, Y.J. & Dziewonski, A.M., 2002. Global variability of transition zone thickness, *J. geophys. Res.*, **107**, doi:10.1029/2001JB000489.
- Gu, Y.J., Ökeler, A. & Schultz, R., 2012. Tracking slabs beneath northwestern Pacific subduction zones, *Earth planet. Sci. Lett.*, **331**, 269–280.
- Heit, B., Yuan, X., Bianchi, M., Kind, R. & Gossler, J., 2010. Study of the lithospheric and upper-mantle discontinuities beneath eastern Asia by *SS* precursors, *Geophys. J. Int.*, **183**, 252–266.
- Herzberg, C. & Gasparik, T., 1991. Garnet and pyroxenes in the mantle: a test of the majorite fractionation hypothesis, *J. geophys. Res.*, **96**, 16 263–16 274.
- Hofmann, A.W., 1997. Mantle geochemistry: the message from oceanic volcanism, *Nature*, **385**, 219–229.
- Houser, C., Masters, G., Flanagan, M. & Shearer, P., 2008. Determination and analysis of long-wavelength transition zone structure using *SS* precursors, *Geophys. J. Int.*, **174**, 178–194.
- Ita, J. & Stixrude, L., 1992. Petrology, elasticity and composition of the mantle transition zone, *J. geophys. Res.*, **97**(B5), 6849–6866.
- Ito, E. & Takahashi, E., 1989. Postspinel transformations in the system Mg_2SiO_4 - Fe_2SiO_4 and some geophysical implications, *J. geophys. Res.*, **94**, 10 637–10 646.
- Ito, E., Akaogi, M., Topor, L. & Navrotsky, A., 1990. Negative pressure-temperature slopes for reactions forming $MgSiO_3$ perovskite from calorimetry, *Science*, **249**, 1275–1278.
- Lawrence, J. & Shearer, P., 2008. Imaging mantle transition zone thickness with *SdS*-*SS* finite-frequency sensitivity kernels, *Geophys. J. Int.*, **174**, 143–158.

- Le Stunff, Y., Wicks, C.W. & Romanowicz, B., 1995. P'P' precursors under Africa: evidence for mid-mantle reflectors, *Science*, **270**, 74–77.
- Li, C., van der Hilst, R.D., Engdahl, E.R. & Burdick, S., 2008. A new global model for P wave speed variations in Earth's mantle, *Geochem. Geophys. Geosyst.*, **9**(5), doi:10.1029/2007GC001806.
- Komatitsch, D. & Tromp, J., 2002a. Spectral-element simulations of global seismic wave propagation—I. Validation, *Geophys. J. Int.*, **149**, 390–412, doi:10.1046/j.1365-246X.2002.01653.x.
- Komatitsch, D. & Tromp, J., 2002b. Spectral-element simulations of global seismic wave propagation—II. Three-dimensional models, oceans, rotation and self-gravitation, *Geophys. J. Int.*, **150**, 303–318, doi:10.1046/j.1365-246X.2002.01716.x.
- Komatitsch, D. & Vilotte, J.P., 1998. The spectral element method: An efficient tool to simulate the seismic response of 2D and 3D geological structures, *Bull. seism. Soc. Am.*, **88**(2), 368–392.
- Kustowski, B., Ekström, G. & Dziewonski, A.M., 2008. Anisotropic shear-wave velocity structure of the Earth's mantle: a global model, *J. geophys. Res.*, **113**, B06306, doi:10.1029/2007JB005169.
- Marone, F., Gung, Y. & Romanowicz, B., 2007. Three-dimensional radial anisotropic structure of the North American upper mantle from inversion of surface waveform data, *Geophys. J. Int.*, **171**, 206–222, doi:10.1111/j.1365-246X.2007.03465.x.
- Nettles, M. & Dziewonski, A.M., 2008. Radially anisotropic shear velocity structure of the upper mantle globally and beneath North America, *J. geophys. Res.*, **113**, B02303, doi:10.1029/2006JB004819.
- Niazi, M. & Anderson, D.L., 1965. Upper mantle structure of western North America from apparent velocity of P waves, *J. geophys. Res.*, **70**, 4633–4640.
- Revenaugh, J. & Jordan, T.H., 1991. Mantle layering from ScS reverberations 2. The transition zone, *J. geophys. Res.*, **96**(B12), 19 736–19 780.
- Ringwood, A.E., 1975. *Composition and Petrology of the Earth's Mantle*, McGraw-Hill, New York.
- Ringwood, A.E., 1994. Role of the transition zone and 660 km discontinuity in mantle dynamics, *Phys. Earth planet. Inter.*, **86**, 5–24.
- Schmerr, N. & Garnero, E., 2006. Investigation of upper mantle discontinuity structure beneath the central Pacific using SS precursors, *J. geophys. Res.*, **111**, doi:10.1029/2005JB004197.
- Schmerr, N. & Garnero, E., 2007. Upper mantle discontinuity topography from thermal and chemical heterogeneity, *Science*, **318**(5850), 623–626.
- Schmerr, N. & Thomas, C., 2011. Subducted lithosphere beneath the Kuriles from migration of PP precursors, *Earth planet. Sci. Lett.*, **311**, 101–111.
- Schubert, G., Turcotte, D.L. & Olsen, P., 2001. *Mantle Convection in the Earth and Planets*, Cambridge University Press, Cambridge.
- Shearer, P.M., 1991. Constraints on upper mantle discontinuities from observations of long-period reflected and converted phases, *J. geophys. Res.*, **96**, 18 147–18 182.
- Simmons, N.A. & Gurrola, H., 2000. Multiple seismic discontinuities near the base of the transition zone in the Earth's mantle, *Nature*, **405**, 559–562, doi:10.1038/35014589.
- Thomas, C. & Billen, M.I., 2009. Mantle transition zone structure along a profile in the SW Pacific: thermal and compositional variations, *Geophys. J. Int.*, **176**, 113–125.
- Tromp, J. *et al.*, 2010. Near real-time simulations of global CMT earthquakes, *Geophys. J. Int.*, **183**, 381–389.
- Vacher, P., Mocquet, A. & Sotin, C., 1998. Computations of seismic profiles from mineral physics: the importance of the non-olivine components for explaining the 660 km depth discontinuity, *Phys. Earth planet. Inter.*, **106**, 275–298.
- Van der Lee, S. & Frederiksen, A., 2005. Surface wave tomography applied to the North American upper mantle, in *Seismic Earth: Array Analysis of Broadband Seismograms*, pp. 67–80, eds Nolet, G. & Levander, A., Geophys. Monogr. Ser. 157, American Geophysical Union, Washington, DC, doi:10.1029/157GM05.
- Vinnik, L., 1977. Detection of waves converted from P to SV in the mantle, *Phys. Earth planet. Inter.*, **15**, 39–45.
- Weidner, D.J. & Wang, Y., 1998. Chemical- and Clapeyron-induced buoyancy at the 660 km discontinuity, *J. geophys. Res.*, **103**, 7431–7441.
- Yuan, H., Romanowicz, B., Fischer, K.M. & Abt, D., 2011. 3-D shear wave radially and azimuthally anisotropic velocity model of the North American upper mantle, *Geophys. J. Int.*, **184**, 1237–1260.
- Zhao, L. & Chevrot, S., 2003. SS-wave sensitivity to upper mantle structure: implications for the mapping of transition zone discontinuity topographies, *Geophys. Res. Lett.*, **30**(11), 1590, doi:10.1029/2003GL017223.

SUPPORTING INFORMATION

Additional Supporting Information may be found in the online version of this article:

Figure S1. Stacks of synthetic seismograms from the 3-D model in which the velocity boundary is shifted (see Fig. 10e), shown for four azimuth and distance bins. The cross marks the predicted arrival time of S₆₆₀S precursor. The number at the top right corner of each panel indicates the number of traces in that stack. When the bin is far away from the velocity boundary, only one precursor with smaller amplitude is seen, whereas when the bin is at or near the boundary, 'double precursors' with larger amplitudes are seen. This shows the artificial 'precursor' cannot be suppressed by stacking.

Figure S2. 'Rose diagrams' (angle histograms) showing the global azimuthal coverage that could possibly be achieved by stacking all SS precursor data before the days of USArray. To compute the ray paths, the earthquakes are all shallow (depth ≤ 75 km) events with $5.8 \leq M_b \leq 7.0$ from the Global CMT catalogue from 1976 to 2004, the stations are all seismometers available from IRIS before the deployment of USArray and the distance range is limited in 100°–160°. The globe is subdivided into 412 nearly equal areas, 10°-radius spherical caps for common SS midpoint stack. Within each cap, the 360° azimuth range is divided into 15° bins for plotting the angle histogram. (a) At each spherical cap (i.e. for each 'rose'), the radius of each 'rose petal' (azimuth bin) is proportional to the number of ray paths sampling that direction, and the maximum radius of each 'rose' is normalized to 1. (b) At each spherical cap, all 'petals' have a radius of 1, with the darkness of the petal's colour indicating the number of traces sampling that direction.

Please note: Wiley-Blackwell are not responsible for the content or functionality of any supporting materials supplied by the authors. Any queries (other than missing material) should be directed to the corresponding author for the article.